

Supporting Information

A Single Model for the Thermodynamics and Kinetics of Metal Exsolution from Perovskite Oxides

Alexander Bonkowski,^[a] Matthew J. Wolf,^[a] Ji Wu,^[b] Stephen C. Parker,^[b] Andreas Klein,^[c]
Roger A. De Souza^{*[a]}

^[a] Institute of Physical Chemistry, RWTH Aachen University, Landoltweg 2, 52074 Aachen, Germany.

^[b] Department of Chemistry, University of Bath, Claverton Down, Bath BA2 7AY, U. K.

^[c] Institute of Materials Science, Technical University of Darmstadt, Otto-Berndt-Str. 3, 64287 Darmstadt, Germany.

Methods

The density functional theory calculations were performed with the Vienna Ab Initio Simulation Package (VASP).^{1–4} Core electrons were described with PAW pseudopotentials.⁵ The following pseudopotentials were chosen, all from the 5.4 Perdew–Burke–Ernzerhof (PBE)^{6,7} set of potentials, as provided by the VASP developers:

Atom	Name of potential	Electrons
Sr	Sr sv	4s ² 4p ⁶ 5s ²
Ti	Ti sv	3s ² 3p ⁶ 3d ² 4s ²
O	O	2s ² 2p ⁴
Ni	Ni	3d ⁸ 4s ²

In order to accurately describe the band gap, we use the hybrid HSE06 exchange–correlation functional.^{8–10} The default value of 25% Hartree–Fock exchange was left unchanged to ensure compatibility with other HSE06 calculations^{11–14} and because the (direct/indirect) computational band gap (3.33 eV/3.73 eV) is sufficiently close to the experimental band gap (3.25 eV/3.75 eV).¹⁵

Collinear spin polarisation as well as aspherical contributions to the gradient corrections inside the PAW spheres were included. Calculations were initialised with high-spin and low-spin configurations and then continued only from the lower-energy state. If the initial calculation revealed the system to have equal spin up/spin down (e.g. all calculations with Ni⁰ or without an Ni in the system), it was continued as a non-spin-polarised calculation to reduce the computational cost.

All calculations were performed under periodic boundary conditions. The plane-wave kinetic energies were truncated at 520 eV for the initial relaxation of the unit cell, yielding a lattice parameter of 3.899 Å. For subsequent calculations, the lattice parameters were kept fixed at a multiple of this value (*i.e.* 15.596 Å for the 4 × 4 × 4 cell) and the plane-wave cutoff was reduced to 400 eV to reduce computational demand. For all supercell calculations with a 4 × 4 × 4 expansion of the cubic unit cell, the *k*-point sampling was performed only at the Gamma point (the unit cell optimisation used a 7 × 7 × 7 *k*-point sampling grid). Atomic positions were optimised until the residual force were below 0.02 eV / Å (0.04 eV / Å for NEB images). Climbing image NEB calculations were performed using the implementation by Henkelman *et al.*^{16,17}

All calculations were carried out in an expansion of the cubic unit cell. This introduces a methodological error,¹⁸ because tetragonal SrTiO₃ is the ground state at 0 K, but this error is negligible in the present case because of the low energy difference of the two polymorphs ($\Delta E < 0.001$ eV per atom with the HSE functional).

For the calculations of the charge-transition levels, corrections accounting for the periodic self-interaction of the charge were applied according to the FNV (Freysoldt, Neugebauer, and Van de Walle) scheme¹⁹ as implemented in the *sxdefectalign* package.²⁰ The energy of an electron was calculated as the sum of VBM (Valence Band Maximum, obtained from a band-structure calculation) and the band gap. The energy corrections were calculated for a total dielectric constant of 6.9, as obtained from our DFT calculation. We note that the value differs from that measured in experiments, but we attribute this to the imaginary soft TO1 phonon frequency present with both PBE and HSE functionals.¹³ We contend that the computational

value of the dielectric constant should be used to obtain the correction term rather than the much higher experimental value, since this is consistent with the actual dielectric response of the material in the calculation.

For the thermodynamic energy calculations, we apply the same corrections as mentioned above. In addition, we apply an HSE-specific correction^{21,22} of +0.85 eV for the energy of a O₂ molecule to account for oxygen over-binding. The procedure to include the effect of the oxygen chemical potential as a function of temperature and pressure is given in the main text.

For all CI-NEB calculations, no charge corrections were applied to obtain the energy barriers.

Energy profiles from CI-NEB calculations

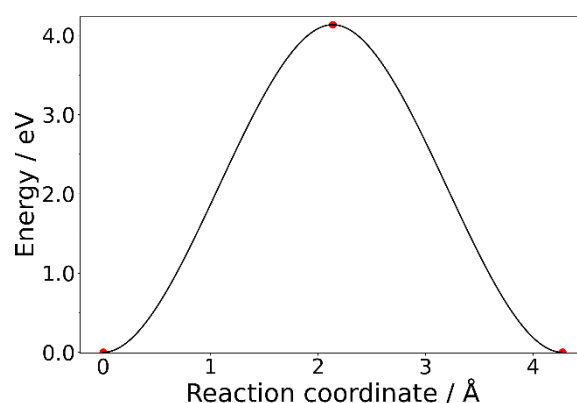


Figure S1 Energy profile of Sr²⁺ migration by a vacancy mechanism in SrTiO₃. The Sr²⁺ ion initially resides on the *A*-site and jumps into an adjacent *A*-site vacancy in $\langle 100 \rangle$ direction.

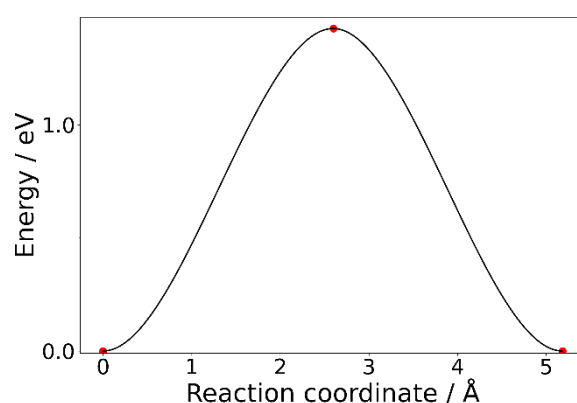


Figure S2 Energy profile of Sr²⁺ migration by a vacancy mechanism with an adjacent v_{Ti} in SrTiO₃. The Sr²⁺ ion initially resides on the *A*-site and jumps into an adjacent *A*-site vacancy in $\langle 100 \rangle$ direction.

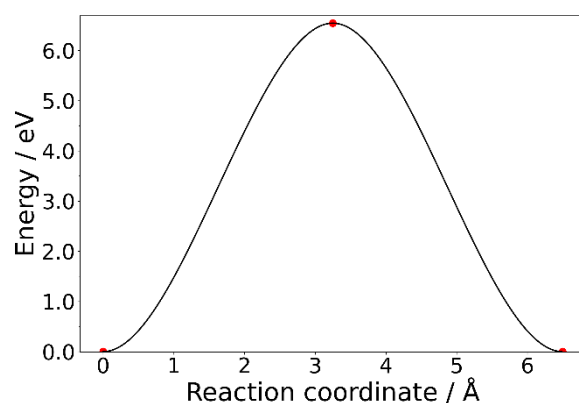


Figure S3 Energy profile of Ti^{4+} migration by a vacancy mechanism in SrTiO_3 . The Ti^{4+} ion initially resides on the B -site and jumps into an adjacent B -site vacancy in $\langle 100 \rangle$ direction.

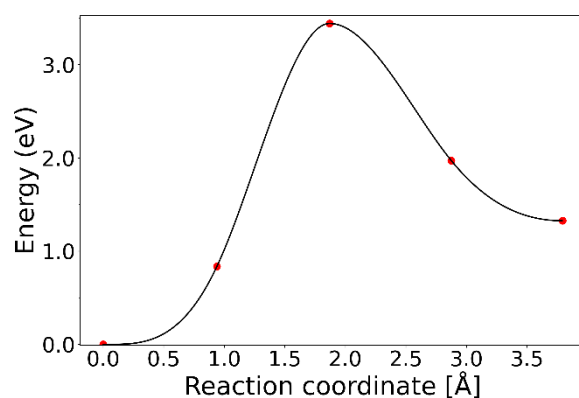


Figure S4 Energy profile of Ti^{4+} migration by a vacancy mechanism with an adjacent v_{Sr} in SrTiO_3 . Only the profile for the ion jump from the initial B -site position to the intermediate, local minimum is shown; the subsequent jump from the local minimum to the final B -site vacancy is mirror-symmetric to the jump shown in the figure.

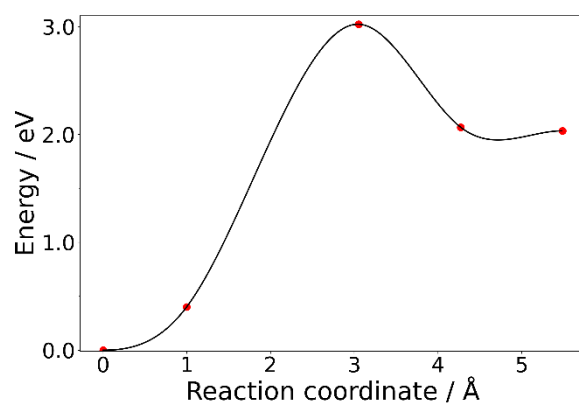


Figure S5 Energy profile of Ni^{4+} migration by a vacancy mechanism with an adjacent v_{Sr} in SrTiO_3 . Only the profile for the jump from the initial B -site position to the intermediate, local minimum is shown; the subsequent jump from the local minimum is mirror-symmetric to the jump shown in the figure.

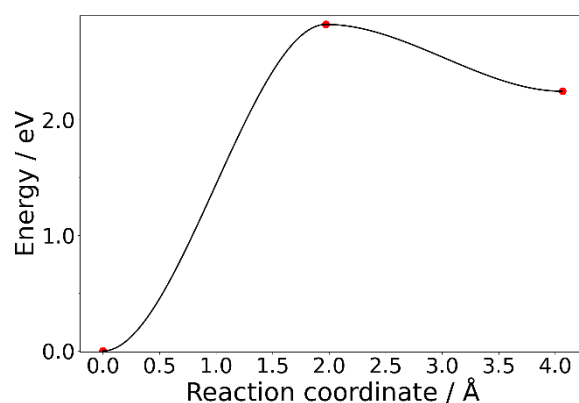


Figure S6 Energy profile of Ni^{3+} migration by a vacancy mechanism with an adjacent v_{Sr} in SrTiO_3 . Only the profile for the jump from the initial B -site position to the intermediate, local minimum is shown; the subsequent jump from the local minimum is mirror-symmetric to the jump shown in the figure.

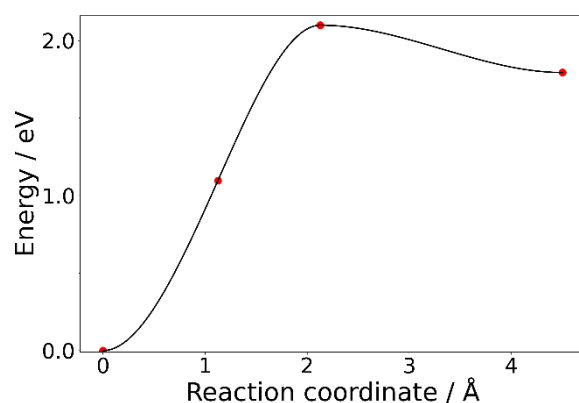


Figure S7 Energy profile of Ni^{2+} migration by a vacancy mechanism with an adjacent v_{Sr} in SrTiO_3 . Only the profile for the jump from the initial B -site position to the intermediate, local minimum is shown; the subsequent jump from the local minimum is mirror-symmetric to the jump shown in the figure.

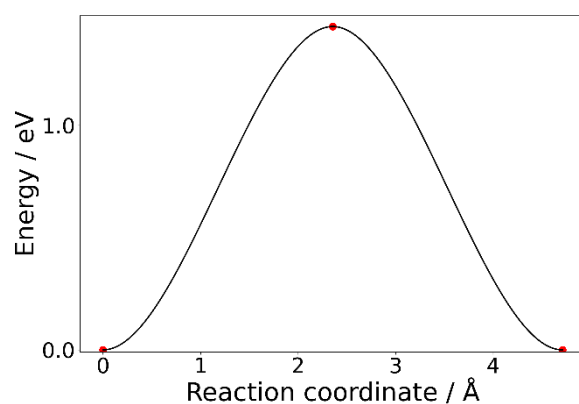


Figure S8 Energy profile of Ni_i^0 migration with an adjacent v_{O} in SrTiO_3 . The Ni_i^0 ion initially resides on the interstitial site and jumps into an adjacent interstitial site in $\langle 110 \rangle$ direction.

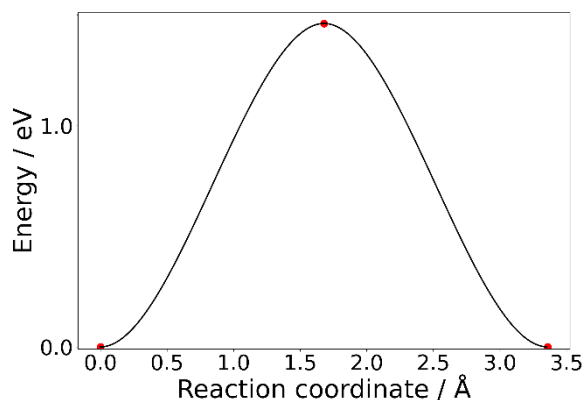


Figure S9 Energy profile of O^{2-} migration by a vacancy mechanism with an adjacent Ni_i^0 in $SrTiO_3$. The O^{2-} ion initially resides on the anion site and jumps into an adjacent anion site in $\langle 110 \rangle$ direction.

References

1. G. Kresse, J. Hafner, *Phys. Rev. B* **1993**, *47*, 558–561.
2. G. Kresse, J. Hafner, *Phys. Rev. B* **1994**, *49*, 14251–14269.
3. G. Kresse, J. Furthmüller, *Phys. Rev. B* **1996**, *54*, 11169–11186.
4. G. Kresse, J. Furthmüller, *Comput. Mater. Sci.* **1996**, *6*, 15–50.
5. P. E. Blöchl, *Phys. Rev. B* **1994**, *50*, 17953–17979.
6. J. P. Perdew, K. Burke, M. Ernzerhof, *Phys. Rev. Lett.* **1996**, *77*, 3865–3868.
7. J. P. Perdew, K. Burke, M. Ernzerhof, *Phys. Rev. Lett.* **1997**, *78*, 1396–1396.
8. J. Heyd, G. E. Scuseria, M. Ernzerhof, *J. Chem. Phys.* **2003**, *118*, 8207–8215.
9. J. Heyd, G. E. Scuseria, M. Ernzerhof, *J. Chem. Phys.* **2006**, *124*, 219906.
10. A. V. Krukau, O. A. Vydrov, A. F. Izmaylov, G. E. Scuseria, *J. Chem. Phys.* **2006**, *125*, 224106.
11. R. Wahl, D. Vogtenhuber, G. Kresse, *Phys. Rev. B* **2008**, *78*, 104116.
12. F. El-Mellouhi, E. N. Brothers, M. J. Lucero, G. E. Scuseria, *Phys. Rev. B* **2011**, *84*, 115122.
13. D. Gryaznov, E. Blokhin, A. Sorokine, E. A. Kotomin, R. A. Evarestov, A. Bussmann-Holder, J. Maier, *J. Phys. Chem. C* **2013**, *117*, 13776–13784.
14. F. Viñes, O. Lamiel-García, K. Chul Ko, J. Yong Lee, F. Illas, *J. Comput. Chem.* **2017**, *38*, 781–789.
15. K. van Benthem, C. Elsässer, R. H. French, *J. Appl. Phys.* **2001**, *90*, 6156–6164.
16. G. Henkelman, B. P. Uberuaga, H. Jónsson, *J. Chem. Phys.* **2000**, *113*, 9901–9904.
17. G. Henkelman, H. Jónsson, *J. Chem. Phys.* **2000**, *113*, 9978–9985.
18. R. A. De Souza, D. Kemp, M. J. Wolf, A. H. H. Ramadan, *J. Phys. Chem. Lett.* **2022**, 11363–11368.
19. C. Freysoldt, J. Neugebauer, C. G. Van de Walle, *Phys. Rev. Lett.* **2009**, *102*, 016402.
20. C. Freysoldt, “sxdefectalign,” can be found under <https://sxrepo.mpie.de/projects/sphinx-add-ons/files>, **2022**.
21. L. Wang, T. Maxisch, G. Ceder, *Phys. Rev. B* **2006**, *73*, 195107.
22. V. L. Chevrier, S. P. Ong, R. Armiento, M. K. Y. Chan, G. Ceder, *Phys. Rev. B* **2010**, *82*, 075122.